Nanoscale

PAPER

View Article Online
View Journal | View Issue

Cite this: *Nanoscale*, 2026, **18**, 974

Anisotropic in-plane thermal transport in monolayer $ReSe_2$ and its modulation through layer control and selenium vacancies: experiment *vs.* theory

Shipra Aswal,[a] Sirsendu Ghosal,[b] Himanshu Murari,[b] Ravinder Chahal,[b] Viliam Vretenár,[c] Ravi K. Biroju,[c,d] Ľubomír Vančo,[c] Subhradip Ghosh [b] and P. K. Giri *[a,b]

Understanding phonon transport and thermal anisotropy in two-dimensional (2D) materials is essential for their integration into electronic and thermal nanoscale devices. In this work, we achieved the growth of large-area, contamination-free monolayer rhenium diselenide ($ReSe_2$) *via* chemical vapor deposition, confirmed by atomic force microscopy and HAADF-STEM imaging. To probe its anisotropic thermal properties, we employed non-contact low-temperature Raman spectroscopy with unpolarized laser excitation to measure its thermal conductivity (κ). We report an exceptionally low value of in-plane thermal conductivity $\kappa \sim 25.2$ Wm^{-1} K^{-1} for the pristine monolayer, the lowest among the TMDs. Critically, we found that the introduction of more selenium vacancies further decreases the thermal conductivity to $\kappa \sim 20.7$ Wm^{-1} K^{-1}. Polarization-dependent Raman analysis reveals a layer-dependent change in the anisotropy ratio, with the ratio decreasing from 6.23 (pristine monolayer) to 4.42 (monolayer with vacancies) and further to 3.82 (trilayer), highlighting the distinct effects of both interlayer interactions and point defects on phonon transport. The decrease of κ with increasing thickness suggests enhanced phonon scattering from structural distortions and weak van der Waals coupling. These findings provide critical insights into how both layer thickness and intrinsic defects such as Se vacancies can be used to modulate anisotropic transport in low-symmetry 2D materials. In addition, we employed density functional theory and Boltzmann transport theory to elucidate the lattice phonon dynamics and thermal transport behaviour of monolayer $ReSe_2$. The computed lattice thermal conductivity (κ_l) exhibits excellent agreement ($\kappa_l^x \approx 21.5$ Wm^{-1} K^{-1} and $\kappa_l^y \approx 23.8$ Wm^{-1} K^{-1}) with the experimental data, thereby providing strong validation for our experimental approach. This work establishes $ReSe_2$ as a strong candidate for thermoelectric and nanoelectronic applications where tunable thermal properties are paramount.

Received 30th August 2025,
Accepted 27th November 2025

DOI: 10.1039/d5nr03668b

rsc.li/nanoscale

1. Introduction

The discovery of two-dimensional (2D) materials has revolutionized materials science, opening doors to groundbreaking applications in optoelectronics,[1] thermoelectrics,[2] molecular sensors,[3] biosensors[4] and energy devices.[5] The remarkable success of graphene, with its unparalleled electronic and thermal properties,[6] has inspired researchers to explore alternative 2D materials that offer tunable properties for diverse applications. While graphene exhibits exceptional thermal conductivity (~4000 Wm^{-1} K^{-1})[6] and high structural stability, its lack of a bandgap and isotropic nature limit its application in semiconductor devices, anisotropic optoelectronics, electronic packaging, and thermal management. This challenge has driven the search for novel 2D materials with tailored thermal[7] and optoelectronic properties,[8] such as hexagonal boron nitride (h-BN), black phosphorus (BP), group VI transition metal dichalcogenides (TMDs), and less-explored group VII chalcogenides.

Unlike graphene and widely studied group VI TMDs, such as MoS_2 and WS_2, which exhibit in-plane isotropic behavior due to their symmetric lattice structure, certain emerging 2D materials, such as BP and group VII TMDs, exhibit intrinsic in-

[a]*Centre for Nanotechnology, Indian Institute of Technology Guwahati, Guwahati 781039, India*
[b]*Department of Physics, Indian Institute of Technology Guwahati, Guwahati 781039, India. E-mail: giri@iitg.ac.in*
[c]*Centre for Nanodiagnostics of Materials, Faculty of Materials Science and Technology, Slovak University of Technology, Vazovova 5, Bratislava, 812 43, Slovakia*
[d]*Nanoelectronics & VLSI Design and Department of Physics - School of Advanced Sciences, Vellore Institute of Technology, Chennai-600127, Tamil Nadu, India*

plane anisotropy.[9] This anisotropy, originating from their low-symmetry crystal structures, is highly desirable for various advanced applications. Among van der Waals (vdW) anisotropic 2D materials, group VII chalcogenides, particularly rhenium dichalcogenides (ReX_2), have garnered significant attention due to their strong structural anisotropy and exceptional optoelectronic properties. ReX_2 crystallizes in a layered structure, with each monolayer consisting of covalently bonded metal and chalcogen atoms arranged in an X–Re–X configuration (where X represents S or Se). However, unlike MoS_2 and WS_2, which exhibit high in-plane symmetry with a hexagonal structure, $ReSe_2$ adopts a distorted 1*T* octahedral configuration with triclinic symmetry (space group: $P\bar{1}$).[10] This unique structural distortion gives rise to inherent in-plane anisotropy in its electronic, optical, and mechanical properties, making it highly promising for polarization-sensitive optoelectronics,[11–13] optical communication systems,[14,15] photonic circuits,[16–18] strain sensors,[19] and direction-dependent electronic devices. Additionally, $ReSe_2$ exhibits significant linear dichroism,[11] further enhancing its potential in optical and photonic technologies. Along with its anisotropic characteristics, $ReSe_2$ possesses excellent air stability,[17] high electron and hole mobilities,[18] ambipolar transport behavior,[20,21] and mechanical flexibility,[22] extending its applications to molecular sensing,[23] photocatalysis,[24,25] ion storage,[26] bioimaging,[27,28] rechargeable batteries,[29] FETs,[18,30] and flexible electronics.[19,31] Furthermore, its strong saturable absorption[14] and polarization-dependent emission[11] make it an attractive candidate for photonic and optoelectronic applications, including polarization-dependent photodetection and tunable light absorption technologies.

Beyond optoelectronic applications, the anisotropic properties of $ReSe_2$ also make it a promising material for thermoelectric energy harvesting. The ability to directly convert heat into electricity *via* the Seebeck effect makes 2D materials attractive for flexible and wearable thermoelectric devices. The energy conversion efficiency of such devices is characterized by the dimensionless figure-of-merit, $ZT = S^2\sigma T/\kappa$, where S is the Seebeck coefficient, σ is the electrical conductivity, T is the temperature, and κ is the thermal conductivity. Since thermal conductivity plays a key role in optimizing ZT, the tunability of κ in $ReSe_2$ offers a pathway for enhancing thermoelectric performance.[32] Given its strong in-plane anisotropy and moderate electrical conductivity, $ReSe_2$ has the potential to serve as an efficient thermoelectric material, bridging the gap between high-performance electronic materials and energy-efficient heat-to-electricity conversion. However, despite the extensive studies on graphene and MoS_2, the anisotropic thermal transport properties of $ReSe_2$ and how they can be controlled remain largely unexplored.

Fabricating high-quality $ReSe_2$ is a significant challenge due to the vast difference in melting points between rhenium (~3180 °C) and selenium (~155 °C). While methods like mechanical exfoliation produce pristine flakes, they are not scalable. Other techniques like liquid-phase exfoliation and solvothermal synthesis sacrifice crystal quality or struggle with precursor control. Chemical vapor deposition (CVD), however, offers a promising solution. It enables large-area, uniform growth with precise control over thickness, morphology, and crystal quality by carefully adjusting the growth parameters like temperature and gas flow. This makes CVD an ideal, scalable method for fabricating 2D $ReSe_2$ for optoelectronic and energy applications. However, while CVD has achieved significant success in growing 2D TMDs like MoS_2[33] and WS_2,[34] extending this level of control to anisotropic materials like $ReSe_2$ on SiO_2/Si remains a challenge. Large-area synthesis is essential for developing flexible, thermally sensitive optoelectronic devices and ensuring compatibility with industrial-scale applications.

To fully understand and optimize $ReSe_2$ for these applications, Raman spectroscopy is an indispensable tool. Polarization-resolved Raman studies have been used to probe the anisotropic vibrational modes of $ReSe_2$, revealing unique phonon behavior linked to its triclinic symmetry.[35] A significant gap remains in understanding how this in-plane anisotropy is affected by layer stacking and the presence of selenium vacancies. Furthermore, while temperature-dependent Raman spectroscopy is a well-established method for gaining insights into phonon–phonon interactions and thermal conductivity, there have been no attempts to apply this to CVD-grown $ReSe_2$ to systematically quantify its layer- and defect-dependent thermal properties. This study fills this gap by utilizing comprehensive Raman measurements—including power-, polarization-, and temperature-dependent analysis—to directly quantify the effects of both layer thickness and selenium vacancies on the anisotropic thermal transport of $ReSe_2$. Furthermore, using first-principles calculations combined with the phonon Boltzmann transport formalism, we investigated the lattice phonon dynamics and thermal transport mechanisms in monolayer $ReSe_2$. To replicate the actual experimental conditions, boundary scattering was incorporated into the simulations, yielding more accurate results.

In this work, we report the large-area synthesis of monolayer and trilayer $ReSe_2$ *via* CVD, ensuring excellent structural and chemical uniformity. The core of our investigation lies in a comprehensive Raman spectroscopic analysis, which includes polarization, power, and temperature-dependent measurements, to understand how the 2D $ReSe_2$ thermal properties can be modulated. We systematically analyzed the anisotropic vibrational modes and thermal conductivity, particularly focusing on the effects of both layer thickness and temperature annealing, which generates Se vacancies. Using a simplified radial heat dissipation model, we quantified the thermal conductivity and anisotropy. To our knowledge, this is the first study to estimate the layer- and defect-dependent in-plane thermal conductivity of CVD-grown $ReSe_2$ using laser excitation, establishing a critical foundation for its use in anisotropic optoelectronics and thermoelectrics. Theoretically predicted thermal conductivity values show excellent agreement with the experimental measurements. We provide a detailed analysis of both harmonic and anharmonic contributions to phonon transport in monolayer $ReSe_2$.

2. Experimental details

2.1. Materials

Rhenium(VI) oxide (ReO_3, 99.9%) was purchased from Alfa Aesar Company. Selenium powder (Se, 99.9%) and NaCl (99.9%) were purchased from Sigma-Aldrich. All chemicals were used without any further purification or alteration.

2.2. CVD growth of 2D $ReSe_2$

We synthesized pristine monolayer $ReSe_2$ (1L-$ReSe_2$) films and few-layer $ReSe_2$ (3L-$ReSe_2$) flakes on SiO_2/Si, along with Se-vacancy-rich monolayer $ReSe_2$ (named 1L-A$ReSe_2$), using a two-zone thermal CVD system. For pristine growth, the substrates were strategically placed upside down above the ReO_3 precursor in the high-temperature zone 2, while the Se powder was kept in a separate, cooler zone 1. High-purity argon (95%) with 5% hydrogen acted as the carrier gas. As shown in Fig. S1 (SI), the process involved a pre-heating phase at 150 °C under 300 sccm Ar to remove moisture and other contaminants, followed by heating to the target growth temperature for 12 minutes—at 650 °C for monolayer synthesis and at 700 °C for few-layer synthesis—before natural cooling. To create a Se-vacancy-rich monolayer (1L-A$ReSe_2$) for modulating the $ReSe_2$ anisotropic properties, we performed a post-growth annealing step. This controlled fabrication approach allowed us to produce high-quality $ReSe_2$ with varying layer thicknesses and defect concentrations, which is essential for our subsequent characterization.

2.3. Sample-transfer method

Efficient and reliable transfer techniques are essential for studying 2D materials on alternative platforms. In this study, we employed a simple yet effective stepwise method to transfer CVD-grown $ReSe_2$ layers from a SiO_2/Si substrate onto a Quantifoil holey carbon Cu grid for HAADF-STEM characterization. A PMMA solution was first drop-cast onto the $ReSe_2$ layer and spin-coated at 1500 rpm for 60 seconds to ensure uniform coverage, followed by baking at 50 °C to solidify the PMMA film. The sample was then immersed in a KOH solution for 3 hours, enabling the detachment of the $ReSe_2$ layer from the SiO_2/Si substrate. The released film was transferred to distilled water to prevent damage and facilitate handling before being carefully placed onto the grid. Finally, the PMMA layer was removed using an extended 24 hour immersion in hot acetone, followed by overnight hot ethanol treatment ensuring minimal residue and enabling atomic-resolution STEM imaging. This extended PMMA removal step is critical for obtaining high-quality, contamination-free atomic-resolution STEM data. The same transfer method was successfully applied to prepare suspended $ReSe_2$ samples on a 300 mesh Cu grid (without carbon coating) for the excitation power-dependent Raman study, demonstrating its versatility. A schematic illustration of the transfer process is provided in Fig. S2 (SI).

2.4. Characterization techniques

The CVD-grown 2D $ReSe_2$ samples were thoroughly analyzed in this study using various characterization tools. An optical microscope attached within a micro-Raman measurement system (LabRam HR800, Horiba) was used for morphological characterization of the as-grown $ReSe_2$. Raman spectroscopy was performed using a LabRam HR800 (Horiba Scientific) system with excitation wavelengths of 514 nm (Ar ion laser) and 633 nm (He–Ne laser). The spectra were collected in a backscattering geometry through a multimode fiber grating (1800 grooves per mm) with a charge-coupled device (CCD) detector. A 100× objective lens provided a spot size of approximately 1 μm, and the laser power was set to 0.5 mW (514 nm) and 1 mW (633 nm). The thickness of $ReSe_2$ was estimated using a non-contact scanning-mode atomic force microscope (AFM) (Cypher, Oxford Instruments) operating in tapping mode, ensuring minimal surface interaction while providing high-resolution topographic data. X-ray Photoelectron Spectroscopy (XPS) was carried out using a PHI 5000 VersaProbe III (Physical Electronics, USA) with a monochromatic K-Alpha X-ray source (1486.7 eV) to analyze the chemical composition and oxidation states of $ReSe_2$. Auger electron spectroscopy and elemental mapping were performed using a Jeol JAMP-9510F Auger microprobe equipped with a hemispherical electron analyzer operating in constant retardation ratio mode with an energy resolution of $\Delta E/E$ = 0.6% with a 10 keV and 10 nA excitation beam. Both incident and emission angles were set to 30°. The atomic structure and crystallinity of $ReSe_2$ were analyzed by HAADF-STEM imaging using a JEOL JEM-ARM200cF aberration-corrected transmission electron microscope operating at 80 kV and equipped with a 100 mm^2 JED-2300 silicon drift detector (JEOL, Japan) for EDS spectroscopy. For STEM imaging, the probe convergence semi-angle was 22 mrad and the beam current was 10.5 pA. HAADF images were obtained using a HAADF detector having inner and outer semi-angles of 68 and 280 mrad, respectively. The samples were transferred onto a Quantifoil holey carbon R2/2 Cu grid (300 mesh) for improved imaging contrast. HAADF-STEM imaging provided insight into the interplanar spacing, structural uniformity, and crystallinity of the as-grown $ReSe_2$. Low-temperature Raman measurements were conducted using a temperature-controlled stage with a 50× objective lens, with liquid nitrogen used as the coolant. Power-dependent Raman spectra were recorded using a 100× objective (NA = 0.9) at varying laser power levels with a 514 nm excitation source. The exact laser power at the sample surface was measured using a commercial power meter (Horiba). The low-temperature and power-dependent measurements were performed on a Linkam stage, without a vacuum.

2.5. Computational details

The first-principles calculations in this work were performed within the framework of density functional theory (DFT)[36,37] as implemented in the Vienna *Ab initio* Simulation Package (VASP).[38] The electron–ion interactions were treated using the projector augmented-wave (PAW) method,[39] and the exchange–correlation energy was described within the Perdew–Burke–Ernzerhof (PBE) generalized gradient approximation (GGA).[40] A plane-wave energy cutoff of 450 eV was employed. For struc-

tural optimization, convergence thresholds of 10^{-7} eV for the total energy and 10^{-3} eV Å^{-1} for the Hellmann–Feynman forces were used. The Brillouin zone was sampled using the Monkhorst–Pack scheme[41] with a 16 × 16 × 1 k-point grid. A vacuum spacing of 20 Å along the z-direction was applied to avoid interaction between periodic images.

The second-order (harmonic) interatomic force constants (IFCs) and phonon dispersions were obtained using the finite-displacement method in the Phonopy package[42] with a 4 × 4 × 1 supercell and a 2 × 2 × 1 k-mesh. The lattice thermal conductivity (κ_l) was calculated by solving the phonon Boltzmann transport equation (BTE) iteratively using the ShengBTE code:[43]

$$\kappa_l^{\alpha\beta} = \frac{1}{k_B T^2 V N} \sum_{\lambda} C_\lambda \nu_\lambda^\alpha \nu_\lambda^\beta \tau_\lambda \quad (1)$$

where V is the unit cell volume, N is the number of q points sampled in the Brillouin zone, C_λ and ν_λ^α are the mode-specific heat and group velocity of phonon branch λ along direction α, and τ_λ is the phonon lifetime. The total lifetime is given by:

$$\frac{1}{\tau_\lambda} = \frac{1}{\tau_\lambda^{anh}} + \frac{1}{\tau_\lambda^{iso}} + \frac{1}{\tau_\lambda^{b}} \quad (2)$$

where τ_λ^{anh} arises from intrinsic three-phonon anharmonic processes, τ_λ^{iso} accounts for elastic phonon scattering due to isotopic mass disorder, and τ_λ^{b} represents diffuse scattering at sample boundaries.

The third-order (anharmonic) IFCs were computed using thirdorder.py.[43,44] For calculations, we have considered a 4 × 4 × 1 supercell and interactions up to the 12th nearest neighbor with a cutoff radius of 4.5 Å. A 2 × 2 × 1 k-mesh was considered for Brillouin zone sampling. The harmonic and anharmonic IFCs were then used in ShengBTE to solve the BTE on a 25 × 25 × 1 q-grid. For 2D compounds, the calculated κ_l was normalized by the factor c/z, where c is the unit cell height (including vacuum) and z is the physical layer thickness.

3. Results and discussion

3.1. Controlled CVD-growth of 1L-ReSe$_2$, 3L-ReSe$_2$ and 1L-AReSe$_2$

The successful CVD growth of high-quality ReSe$_2$ films depends on the precise control of key parameters, including growth temperature, carrier gas composition, precursors, and substrate positioning. Our process was performed in a double-zone tube furnace using freshly cleaned SiO$_2$/Si as the growth substrate, with an Ar/H$_2$ mixture as the carrier gas, as illustrated schematically in Fig. 1(a). The growth mechanism involved the decomposition of ReO$_3$ into gaseous Re$_2$O$_7$ and less volatile ReO$_2$[45]

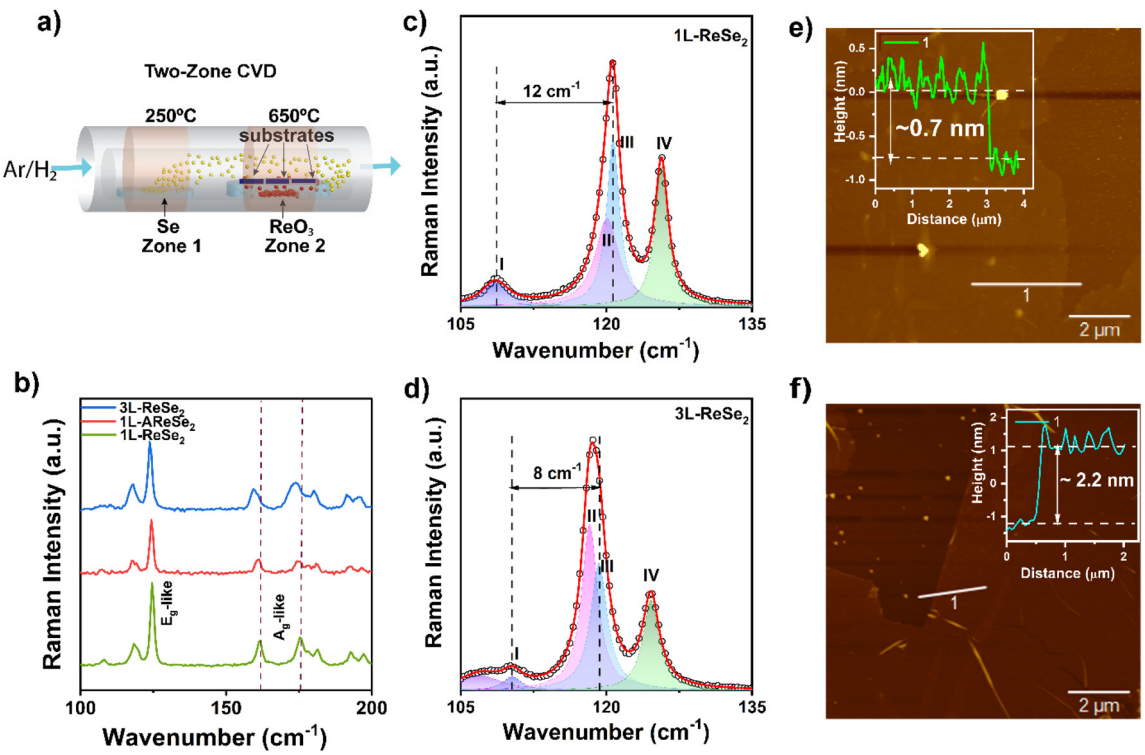

Fig. 1 (a) Schematic illustration of the thermal CVD setup used for synthesizing 2D ReSe$_2$. (b) Raman spectra of 1L-ReSe$_2$, 1L-AReSe$_2$, and 3L-ReSe$_2$ under 514 nm excitation showing the Raman shift with layer thickness and defect integration. (c and d) The deconvoluted Raman spectra of 1L-ReSe$_2$ and 3L-ReSe$_2$ under 633 nm excitation showing mode separation of 12 cm^{-1} and 8 cm^{-1}, respectively, between vibrational modes I and III, highlighting the layer-dependent phonon interaction. (e and f) AFM height profile analyses of 1L-ReSe$_2$ and 3L-ReSe$_2$, with thicknesses of ~0.7 nm and ~2.2 nm, respectively.

around 400 °C, which then reacted with selenium vapor in the presence of H_2 to form $ReSe_2$ nucleation sites:[46]

$$Re_2O_7(g) + ReO_2(g) + Se(g) + H_2 \rightarrow ReSe_2(s) + H_2O + H_2Se.$$

The substrate temperature is a critical factor in controlling the morphology and quality of the $ReSe_2$ flakes. We achieved a monolayer $ReSe_2$ film at an optimized substrate temperature of 650 °C with a growth duration of 12 minutes and a pressure of 10 mbar. Deviations from this temperature were found to significantly alter the growth outcome. As shown in Fig. S3 (SI), a lower temperature of 600 °C resulted in insufficient nucleation energy, leading to the formation of smaller nanoparticles. Conversely, a higher temperature of 700 °C led to thicker, few-layer flakes due to increased reaction rates and a higher material supply. Precise control over temperature, pressure, and gas flow was essential for achieving a uniform, high-quality monolayer film, as any deviation could lead to either incomplete growth or excessive material deposition. To modulate the thermal properties of the material, we intentionally introduced selenium vacancies. This was achieved by a slow ramp heating of the pristine monolayer sample in the same CVD furnace. The sample was annealed at 400 °C for 20 minutes under a continuous 10 sccm Ar flow, which created a significant concentration of Se vacancies.

3.2. Structural and morphological analysis of 2D $ReSe_2$

Large-area 2D $ReSe_2$ films were successfully grown on SiO_2/Si substrates using a CVD system, as schematically illustrated in Fig. 1(a). The as-grown $ReSe_2$ exhibited full coverage growth on the substrate, demonstrating the scalability and high-quality growth crucial for large-area applications. The successful synthesis of 1L-$ReSe_2$, 3L-$ReSe_2$ and 1L-A$ReSe_2$ was confirmed by Raman spectroscopy with characteristic E_g-like and A_g-like vibrational modes observed under 514 nm laser excitation,[47,48] as shown in Fig. 1(b). The full Raman spectrum, displaying all 18 deconvoluted phonon modes characteristic of 2D $ReSe_2$,[49] is presented in Fig. S4 and further detailed in Table S1, along with their mode number.

Unlike 2D MoS_2, where Raman peaks can be distinctly assigned to pure E_g and A_g modes, 1L-$ReSe_2$ exhibits a more complex vibrational structure due to its lower triclinic symmetry 1*T* distorted crystal structure. As a result, phonon modes are classified as E_g-like or A_g-like based on their dominant vibrational characteristics. The Raman peak at 124.7 cm^{-1} is identified as an E_g-like mode, primarily exhibiting in-plane vibrations, while the peaks at 161.5 cm^{-1} and 175.4 cm^{-1} correspond to A_g-like modes, characterized by their predominant out-of-plane vibrational components[45] (Fig. S4(a)). As shown in Fig. 1(c), under 633 nm laser excitation, the separation between modes I and III remains approximately 12 cm^{-1},[49] a characteristic feature of 1L-$ReSe_2$, indirectly confirming the monolayer growth. In contrast, these respective modes of separation reduce to 8 cm^{-1} for 3L-$ReSe_2$,[49] as shown in Fig. 1(d), showing layer-dependent phonon dynamics. AFM height profile analysis further validates the monolayer nature of $ReSe_2$, as shown in Fig. 1(e), with a measured thickness of ~0.7 nm,[48] which is consistent with previously reported values for monolayer $ReSe_2$. Fig. 1(f) depicts a sample thickness of approximately 2.2 nm, indicating 3L-$ReSe_2$.

The Raman modes of the 3L-$ReSe_2$ samples exhibit a marginal redshift and significant broadening in Raman modes compared to the monolayer samples (Table S1 (SI)). This shift is much less significant than in other TMDs due to the presence of weak interlayer vdW interactions. The reduced interlayer coupling in $ReSe_2$ arises from its larger interlayer spacing (~0.7 nm) and unique structural characteristics, leading to minimal frequency shifts in Raman modes as the number of layers increases. Similar behaviour was observed in other VII TMDs with weak interlayer coupling,[50] where only minor thickness-induced frequency shifts are observed in its Raman modes.

The observed redshift in Raman peaks with increasing layer number results from a balance between two competing effects: (i) vdW forces, which tend to stiffen the lattice and induce a blueshift, and (ii) long-range Coulomb interactions, which lead to increased Coulomb screening with additional layers, softening the atomic vibrations and causing a redshift. In $ReSe_2$, the weak interlayer vdW interaction is insufficient to dominate the layer-dependent phonon behavior, allowing the Coulomb screening effect to prevail, resulting in a redshift of most Raman modes.[51] Comparatively, WSe_2, which has a similar atomic mass to $ReSe_2$, exhibits significantly stronger interlayer coupling,[52] leading to more pronounced Raman shifts. The additional optical phonon modes align well with theoretical predictions and previously reported experimental values, as detailed in Table S1 (SI). A noticeable redshift in the Raman modes of monolayer $ReSe_2$ is attributed to marginal n-type doping[53,54] in our as-grown sample.

A clear red shift and spectral broadening were observed in the Raman spectrum of the annealed 1L-A$ReSe_2$ sample compared to the pristine 1L-$ReSe_2$ (Fig. 1(b)). This is predominantly a result of the significant n-type doping effect caused by the introduction of Se vacancies. The presence of these vacancies is directly supported by the observed shifts in the Raman modes as detailed in Table S1 (SI), particularly in the A_g-like vibrational mode.

3.3. XPS and Auger spectroscopy analysis

The chemical composition and stoichiometry of the $ReSe_2$ film were thoroughly examined using XPS analysis. The survey scan spectrum shown in Fig. S5(a) confirms the synthesis of $ReSe_2$ using ReO_3 and Se precursors, indicated by the presence of characteristic peaks for rhenium and selenium. All binding energy values were referenced to the carbon peak at 284.8 eV,[55] as shown in Fig. S5(b). High-resolution XPS spectra provided further insight into the sample chemical state. The Re 4f spectrum in Fig. 2(a) shows two prominent peaks at 41.7 eV and 44.1 eV with a splitting of 2.4 eV, corresponding to Re $4f_{7/2}$ and Re $4f_{5/2}$,[56] respectively, associated with the Re^{4+} oxidation state. Similarly, the Se 3d spectrum in Fig. 2(b) displays a doublet

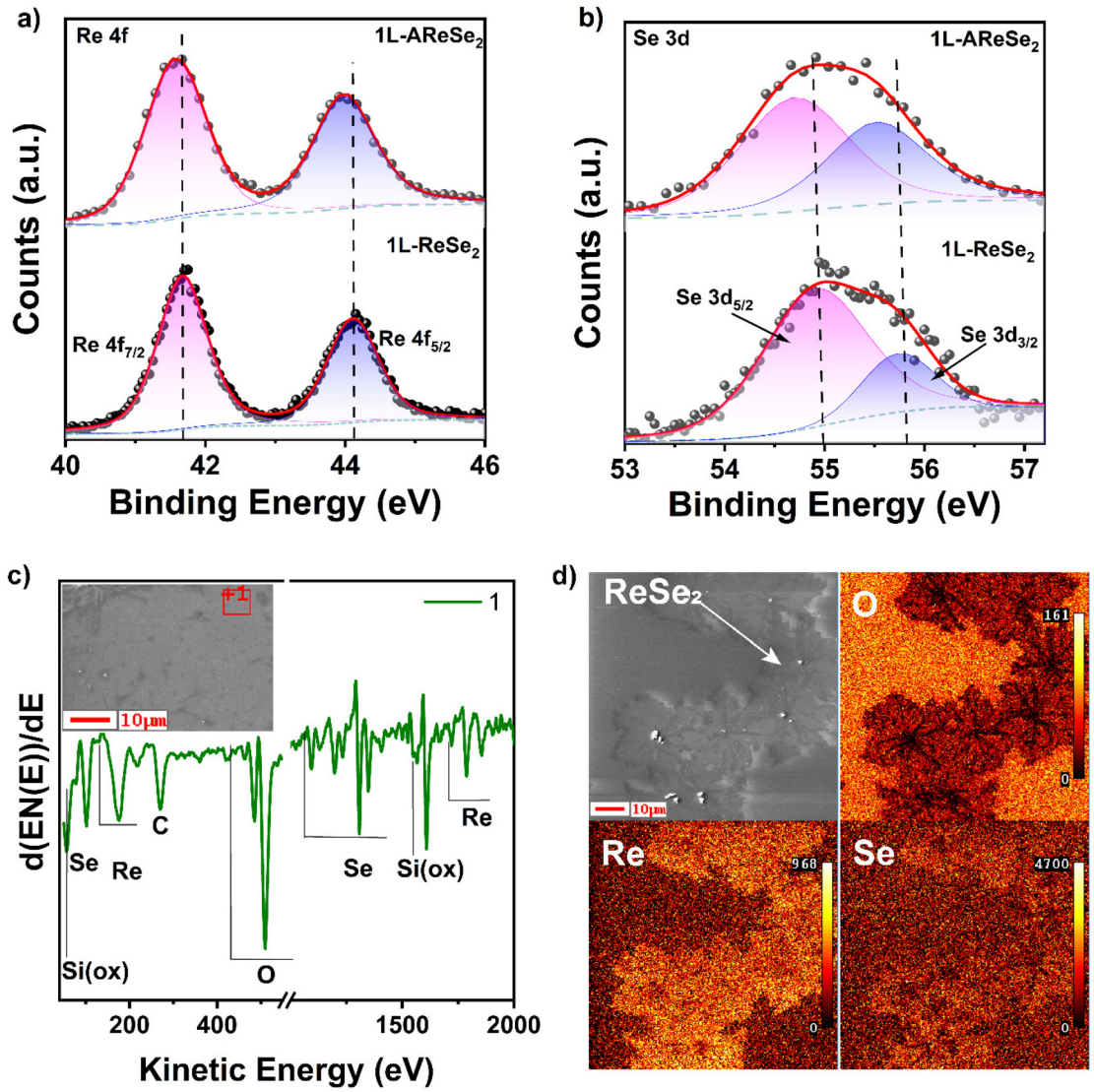

Fig. 2 (a and b) High-resolution core-level XPS spectra of Re and Se in 1L-$ReSe_2$ and 1L-$AReSe_2$. (c) Auger spectra of the as-grown $ReSe_2$ in the marked region shown in the inset. (d) Auger elemental mapping of the as-grown 1L-$ReSe_2$, showing the distribution of Re and Se, with regions lacking these elements exhibiting enhanced oxygen signals arising from the SiO_2 substrate.

with a splitting of 0.9 eV with peaks at 54.9 eV and 55.8 eV, corresponding to Se $3d_{5/2}$ and Se $3d_{3/2}$, respectively.[23] These peaks confirm the Se^{2-} reduction state, validating the formation of $ReSe_2$. Together, these results underscore the high quality of the $ReSe_2$ film synthesized *via* the CVD method. To quantify the stoichiometry, the Se to Re atomic ratio was calculated using the formula:

$$\frac{\mathrm{Se}}{\mathrm{Re}} = \frac{\sum \frac{A_{\mathrm{Se}_x}}{S_{v(\mathrm{Se}_x)}}}{\sum \frac{A_{\mathrm{Re}_x}}{S_{v(\mathrm{Re}_x)}}},$$

where A_x is the area under the fitted curve for the x-orbital and S_{vx} is the corresponding sensitivity factor.

The calculated Se/Re ratio of 1.96 closely aligns with the anticipated stoichiometric value of 2.0, showing the presence of marginal intrinsic Se vacancies in 1L-$ReSe_2$. In contrast, the annealed 1L-$AReSe_2$ sample showed significant changes consistent with defect formation. As shown in Fig. 2(a and b), the binding energy of the core Re 4f spectrum of 1L-$AReSe_2$ slightly decreased, shifting to 41.5 eV and 43.9 eV, while the Se 3d peaks shifted to 54.7 eV and 55.5 eV. Concurrently, the Se/Re ratio decreased significantly to 1.56. Furthermore, the FWHM of both the core Re 4f and Se 3d XPS spectra increased, as detailed in Table S2. These changes—including the decreased binding energies, the reduced Se/Re ratio, and the increased spectral broadening—all provide compelling evidence for the abundant formation of selenium vacancies in the annealed 1L-$AReSe_2$, modulating its crystal structure.

Auger electron spectroscopy of $ReSe_2$ grown on SiO_2/Si substrates provides a detailed understanding of the elemental composition of the material system. The characteristic Auger

transitions observed for rhenium and selenium reveal their presence in the as-grown sample, as shown in Fig. 2(c). For Re, the dominant Auger transitions identified include the MNN peaks at 1787 eV and 1853 eV, as well as the NVV transition at 173 eV.[57] These features confirm the presence of Re within the $ReSe_2$ structure. Se exhibits multiple prominent Auger peaks, including Se LMM transitions present at 1088 eV, 1202 eV, 1307 eV, and 1346 eV, along with an MVV transition at 101 eV.[57] In addition to the signals from Re and Se, substrate-related transitions are also observed. The peaks at 1565 eV and 1613 eV correspond to Si KLL transitions and the peak at around 75 eV corresponds to Si LVV transitions, clearly indicating the presence of Si from the underlying Si dioxide substrate.[58] Furthermore, the peaks near 515 eV are attributed to oxygen, indicative of oxygen species and corroborating the presence of SiO_2 on the substrate surface.

The elemental analysis performed using AES, shown at the marked position, as presented in the inset of Fig. 2(c), shows an elemental ratio of Re to Se of 1.96, which is fully consistent with the elemental composition observed in the XPS data. The AES elemental mapping analysis confirms the presence of Re, Se, and O, affirming the successful growth of $ReSe_2$ on the SiO_2/Si substrate, as shown in Fig. 2(d). The oxygen is from the substrate, and the signal exponentially decreases with film thickness, vanishing in thicker parts (approx. 3–5 nm).

3.4 STEM analysis

The large-area monolayer $ReSe_2$ film is grown by the lateral coalescence of multiple single-crystalline domains that nucleate at different sites. The SAED pattern near the grain boundary shows its polycrystalline nature (Fig. S6(a)), while the single-crystalline grains/domains are evident from the SAED pattern shown in Fig. S6(b). The HAADF-STEM image of the CVD-grown 1L-$ReSe_2$ film is displayed in Fig. 3(a), revealing its distorted octahedral 1*T* (1*T*′) crystal structure. This structure is depicted schematically from a side view (along the *a* axis) in Fig. 3(b) and a top-down view (in the *ab* basal plane) in Fig. 3(d). Fig. 3(c) shows the filtered atomic resolution HAADF *Z*-contrast STEM image of freestanding monolayer $ReSe_2$ grown by our CVD process, showing the lattice parameters. A notable structural feature of the 1*T*′ phase $ReSe_2$ is that every four Re atoms form a parallelogram Re_4 cluster, and these Re_4 clusters interconnect to form quasi-one-dimensional (quasi-1D) chains through intercluster Re–Re bonds, as shown in the schematic in Fig. 3(e). As depicted in Fig. 3(c), the interplanar spacings of ~0.31 and ~0.39 nm are associated with the (100)

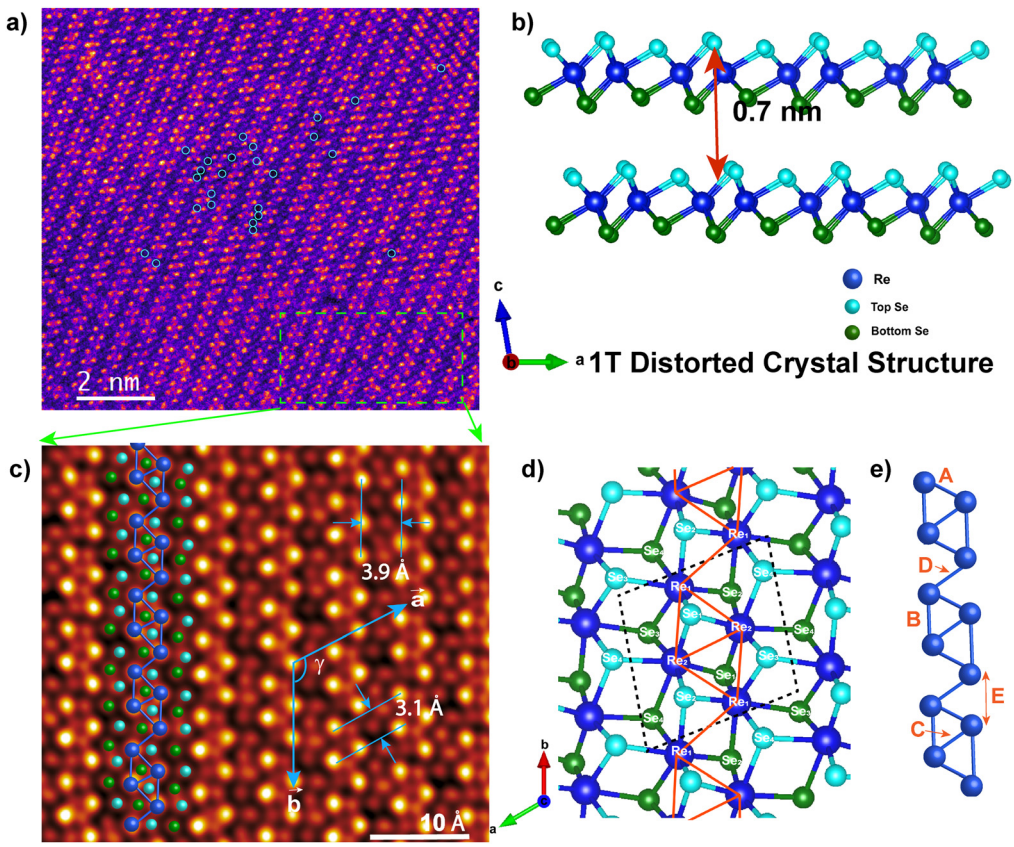

Fig. 3 (a) A STEM HAADF image of the transferred $ReSe_2$ monolayer showing the crystal structure and the presence of Se vacancies (encircled points). (b) Schematic representation of the $ReSe_2$ 1*T* distorted crystal structure along the *a* axis. (c) Atomic-resolution HAADF-STEM image of monolayer $ReSe_2$ showing typical Re–Re spacings and lattice parameters. (d) Schematic of the structure showing different equivalent positions of rhenium and selenium atoms in the 1*T* distorted crystal structure in the basal plane; the absence of particular Se atoms at the respective sites leads to Se_1-, Se_2-, Se_3-, and Se_4-types of vacancies. (e) Schematic representation of Re_4 clusters interconnecting to form a quasi-one-dimensional chain.

and (010) crystallographic planes of triclinic $ReSe_2$, which match well with previously reported values.[59] The STEM-ADF image (Fig. 3(a)) highlights the presence of Se vacancies (indicated by cyan circles). There is the presence of Se_1-, Se_2-, Se_3-, Se_4-type selenium sites,[59] as evident from the schematics in Fig. 3(d). Line profiling of the HAADF-STEM image along the *b* [010] direction in Fig. S7(a and b) (SI) reveals the distribution of Re and Se atoms and confirms the existence of Se_2 type-vacancies (V_{Se_2}) along the *b*[010] direction.[59] The composition of the sample was further analyzed using EDS elemental mapping *via* TEM, as shown in Fig. S7(c) (SI), which gives a Re to Se ratio of 1.95. The presence of intrinsic Se vacancies supports the measured atomic ratio of 1.95. The observed value of the Se to Re ratio matches the XPS data. The line profiles of Re atoms along the [100] and [010] directions are used to estimate lattice spacings *a* and *b*, respectively. The lattice parameters obtained from the line profiles of the STEM-ADF (Fig. 3(c)) image are a = 6.76 Å, b = 6.66 Å, and γ = 118.6°, which are consistent with those obtained from calculations within the accuracy of the experimental data.[59,60]

The Re–Re spacing along the 1D parallelogram Re_4 cluster and the lattice spacing obtained using atomic resolution STEM data, namely spacings A, B, C, D, and E, as shown in Fig. 3(e), and the line profile, are presented in Table 1. The measured experimental values of the Re–Re spacing match well with the theoretical ones within the error limits of 0.1 Å.[60]

3.5. Low-temperature Raman studies

A detailed low-temperature Raman study was conducted on CVD-grown 1L-$ReSe_2$, 1L-A$ReSe_2$, and 3L-$ReSe_2$, in a temperature range of 93–293 K, to examine the temperature dependence of the vibrational modes of 2D $ReSe_2$ and its modulation with the layer stacking and Se vacancies. The low-temperature Raman spectra, depicted in Fig. 4(a,–c), reveal distinct trends in the characteristic Raman modes, specifically the A_g-like and E_g-like peaks[35,56] of 1L-$ReSe_2$, 1L-A$ReSe_2$, and 3L-$ReSe_2$, respectively. The schematics of E_g-like mode vibration and A_g-like mode vibration are shown in Fig. S8 (SI), respectively. A pronounced blue shift of these peaks was observed as the temperature decreased. This shift is attributed to the anharmonicity in lattice vibrations, which arises due to reduced phonon–phonon interactions at lower temperatures.[61–63] The Raman spectra were carefully analyzed by fitting with a Lorentzian line shape function to ensure precise identification of the peak positions. To gain deeper insights into the anharmonic effects within the crystal lattice and assess the thermal stability of monolayer $ReSe_2$ under varying temperature conditions, we determined the temperature coefficient (α) by employing a linear relationship:

$$\omega = \omega_o + \alpha T.$$

This gives a correlation between the frequency ω of the Raman mode and the temperature (T). The parameters ω_o and

Table 1 Comparison of experimental and theoretical lattice parameters, along with typical Re–Re spacings in monolayer $ReSe_2$

	a/Å	*b*/Å	*γ*/°	*A*/Å	*B*/Å	*C*/Å	*D*/Å	*E*/Å
Experimental	6.76	6.66	118.6	2.85	2.92	2.67	3.02	3.75
Theoretical	6.77	6.66	118.9	2.85	2.89	2.76	3.03	3.78

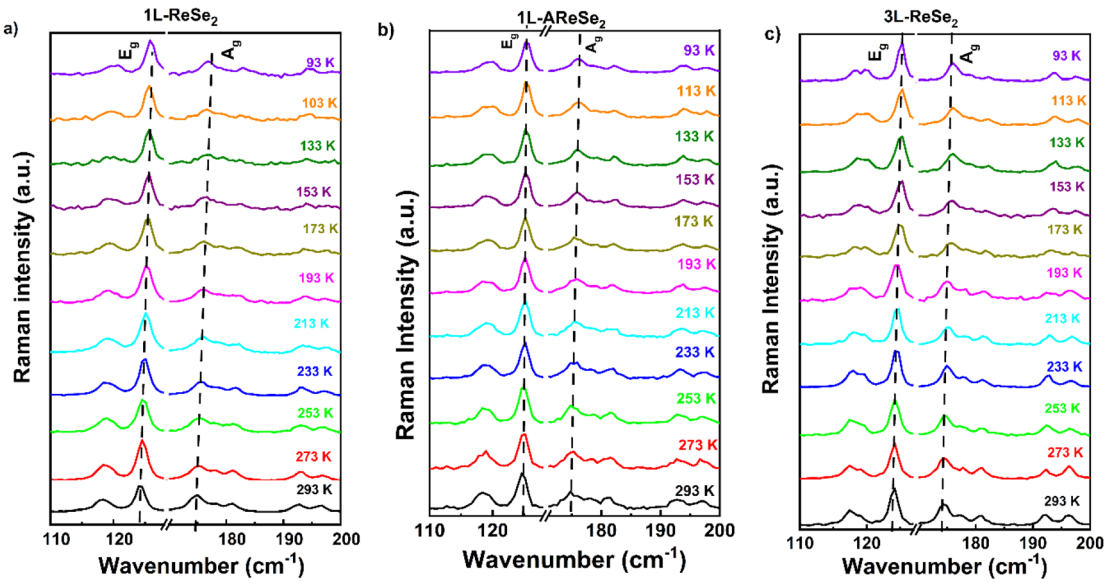

Fig. 4 Temperature-dependent Raman spectra of (a) monolayer $ReSe_2$, (b) annealed monolayer $ReSe_2$ and (c) trilayer $ReSe_2$ showing a systematic blue-shift with a decrease in the temperature in each case.

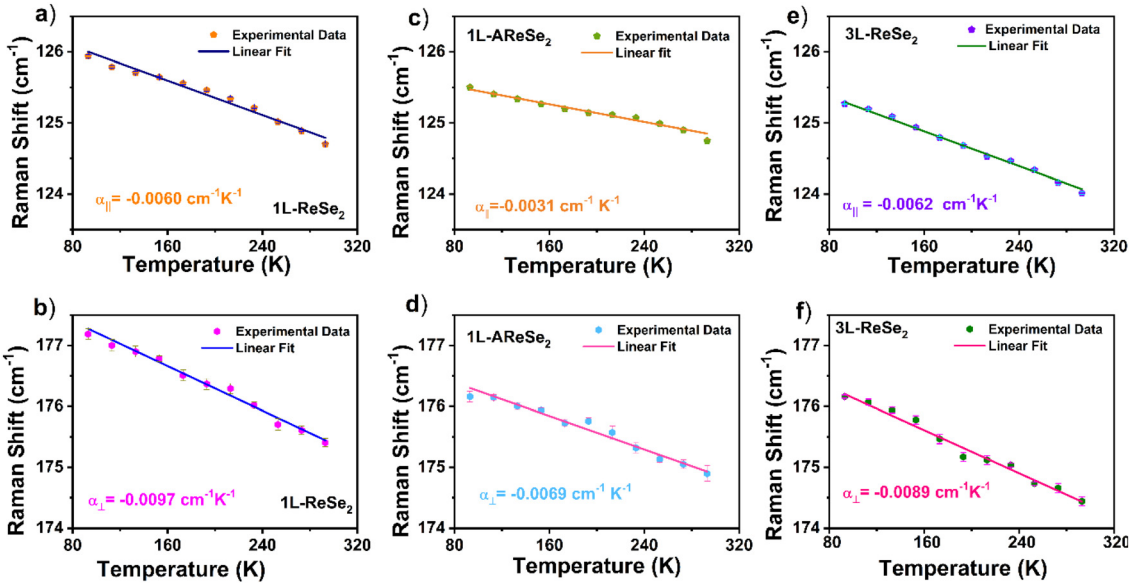

Fig. 5 Temperature-dependent Raman shifts of the E_g-like mode at ~124 cm^{-1} for (a) 1L-$ReSe_2$, (c) 1L-A$ReSe_2$, and (e) 3L-$ReSe_2$. Temperature-dependent Raman shifts of the A_g-like mode at ~175 cm^{-1} for (b) 1L-$ReSe_2$, (d) 1L-A$ReSe_2$, and (f) 3L-$ReSe_2$.

α represent the frequency at absolute zero temperature and the first-order temperature coefficient, respectively. From the linear plot in Fig. 5(a) and (b), we obtained values of the first-order temperature coefficient (α) as −0.0060 ± 0.00032 cm^{-1} K^{-1} and −0.0097 ± 0.00030 cm^{-1} K^{-1} for the E_g-like mode at 124.7 cm^{-1} and the A_g-like mode at 175.4 cm^{-1}, respectively, for 1L-$ReSe_2$. Similarly, in the case of 1L-A$ReSe_2$, we obtained values of the first-order temperature coefficient (α) as −0.0031 ± 0.00013 cm^{-1} K^{-1} for the E_g-like mode at 124.7 cm^{-1} and −0.0069 ± 0.00033 cm^{-1} K^{-1} for the A_g-like mode at 174.8 cm^{-1}, as shown in Fig. 5(c and d), respectively. This considerable reduction in the temperature coefficients in the annealed sample is a direct consequence of the Se vacancies introduced during the annealing process. These vacancies disrupt the crystal lattice and scatter phonons, which in turn significantly reduce phonon–phonon interactions and alter the thermal transport in the material. Similarly, in the case of 3L-$ReSe_2$, we obtained values of the first-order temperature coefficient (α) as −0.0062 ± 0.00044 cm^{-1} K^{-1} for the E_g-like mode at 123.9 cm^{-1} and −0.0089 ± 0.00031 cm^{-1} K^{-1} for the A_g-like mode at 173.4 cm^{-1}, as shown in Fig. 5(e and f), respectively. The results indicate a subtle variation in the temperature coefficients (TECs) with layer stacking, reflecting changes in phonon–phonon interactions that occur as interlayer coupling becomes a more significant factor in the trilayer system.

In CVD-grown $ReSe_2$, TECs exhibit distinct behaviors for in-plane (E_g-like) and out-of-plane (A_g-like) vibrational modes as the number of layers increases. Specifically, the TEC for the in-plane E_g-like mode slightly increases with additional layers, while the TEC for the out-of-plane A_g-like mode decreases. This phenomenon aligns with observations in other anisotropic 2D materials.[62] The decrease in the TEC of the out-of-plane A_g-like mode with increasing layers can be attributed to enhanced interlayer vdW interactions. These interactions restrict atomic vibrations perpendicular to the plane, reducing anharmonic effects and, consequently, a lower TEC was obtained. In contrast, the in-plane E_g-like mode is less affected by interlayer coupling, allowing its TEC to increase slightly with additional layers. In summary, the observed variations in TECs for the in-plane and out-of-plane modes in $ReSe_2$ with increasing layer numbers are primarily due to the interplay between interlayer vdW interactions and the inherent anisotropic properties of 2D materials.[62,64] The relatively low values of α suggest that $ReSe_2$, as compared to other TMDs (shown in Table S3 (SI)), exhibits strong lattice stability and weak anharmonic effects, making it a promising material for temperature-sensitive applications.

3.6. In-plane anisotropic ratio (AR)

Different optical methodologies have been used to evaluate the anisotropic ratios in anisotropic 2D by systematically rotating the polarization angle (θ). As the polarization angle changes, the intensity of the characteristic Raman peaks varies with the structure of anisotropic materials. Using polarized excitation, it was reported that $ReSe_2$ has an anisotropic ratio of up to ~2.62 from the absorbance peak at 800 nm.[65] However, to the best of our knowledge, there are no prior reports quantifying the anisotropic ratio of monolayer $ReSe_2$ using laser-based excitation, nor are there systematic studies on how this ratio varies with defect content or layer stacking. In our study, we employed polarized Raman spectroscopy to quantify the anisotropic ratio in CVD-grown 2D $ReSe_2$. The schematic of the polarization configuration of the polarized Raman measurement is displayed in Fig. 6(a). To investigate the structural anisotropy of $ReSe_2$, the experimental setup begins with a verti-

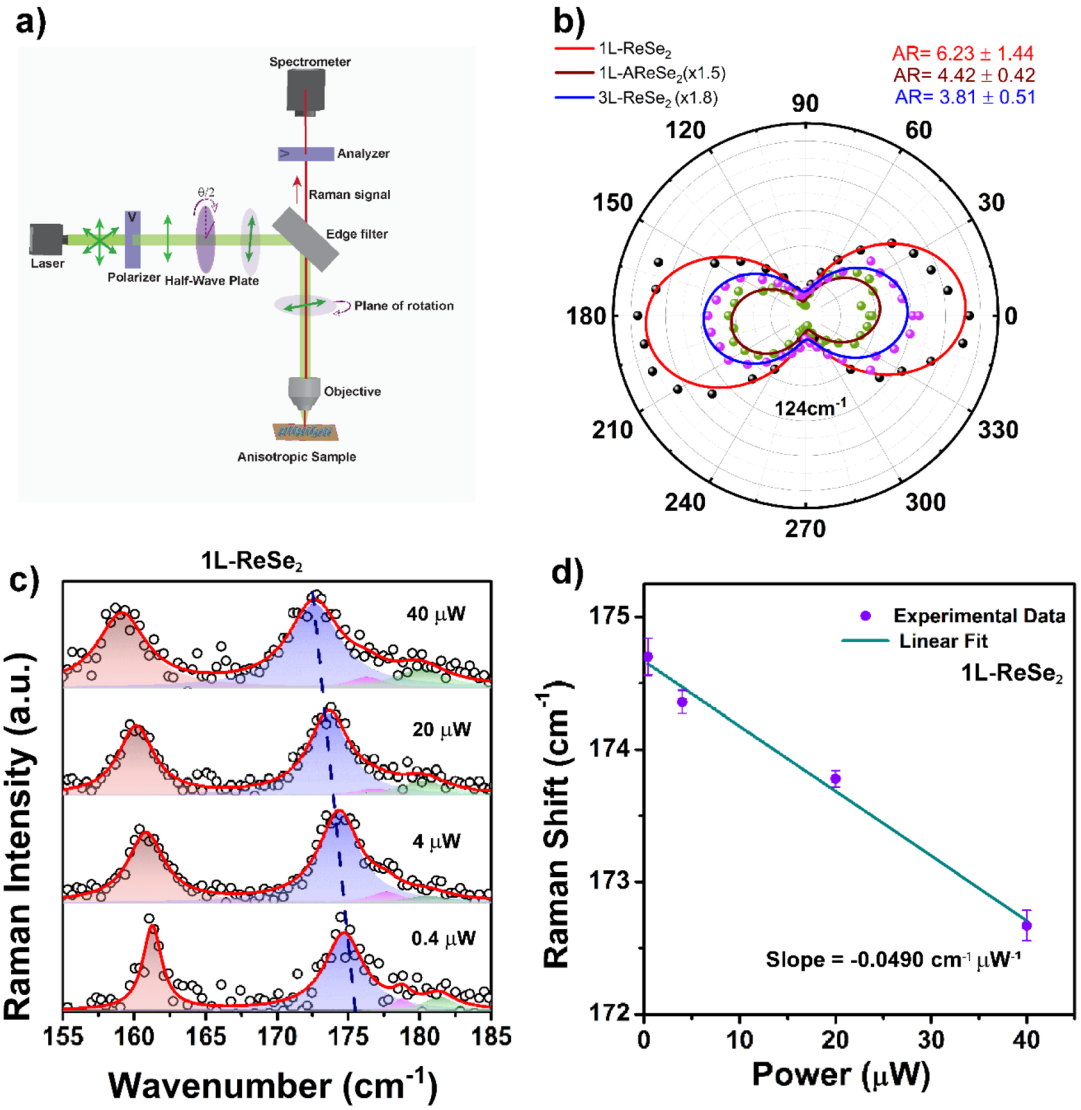

Fig. 6 (a) Schematic of polarization-dependent Raman measurement on 2D $ReSe_2$. (b) Polar plots of the variation of intensity of the E_g-like mode at ~124 cm^{-1} for 1L-$ReSe_2$, 1L-A$ReSe_2$, and 3L-$ReSe_2$. (c) Power-dependent Raman spectra of monolayer 1L-$ReSe_2$. (d) Raman shifts of the A_g-like mode at ~175 cm^{-1} with variation in laser power for 1L-$ReSe_2$.

cally plane-polarized laser beam that passes through a half-wave plate. This plate is positioned in the common optical path, allowing it to control the polarization of both the incoming and outgoing light. By rotating the fast axis of the half-wave plate by an angle of $\theta/2$, the polarization plane of the incident laser light is precisely rotated by an angle θ. This rotated light is then focused onto the sample. The backscattered Raman signal from the sample is collected and passed through an analyzer, which is fixed in a parallel configuration to the polarizer (vv configuration). Finally, the signal enters a spectrometer, where its intensity is measured. The variation in the detected intensity as the angle θ is changed is a direct result of the anisotropic crystal structure of $ReSe_2$, providing a clear measurement of its optical anisotropic behaviour.

To quantify this variation, we used Lorentzian line shapes to deconvolute the Raman peaks and accurately determine their intensity at each angle (θ). The polarization-dependent Raman spectra of 1L-$ReSe_2$, 1L-A$ReSe_2$, and 3L-$ReSe_2$ are displayed in Fig. S9 (SI). The anisotropic ratio is defined as the ratio of the maximum intensity to the minimum intensity of the fitted in-plane mode intensity variation, given by $I_{vv} = |a\cos^2\theta + d\sin^2\theta + 2bd\cos\theta\sin\theta|^2$,[21] where a, b, and d are constant parameters. Using this methodology, we found a giant anisotropic behaviour in monolayer $ReSe_2$, with a calculated ratio of 6.23 ± 1.44, as depicted in Fig. 6(b). This value is significantly higher than that reported from optical absorption measurements, highlighting the profound anisotropy in the phonon dynamics of 1L-$ReSe_2$. Furthermore, we explored how structural defects in 1L-$ReSe_2$ influence this anisotropy. Selenium vacancies were introduced into 1L-$ReSe_2$ through controlled annealing, which led to a substantial reduction in the anisotropic ratio to 4.42 ± 0.42 in 1L-A$ReSe_2$. This

reduction is attributed to the phonon scattering caused by vacancies, which disrupts the lattice periodicity and weakens the directional vibrational contrast. We also extended our measurements to 3L-$ReSe_2$, where the anisotropic ratio was found to be 3.82 ± 0.50. This notable decrease compared to the monolayer case is likely due to the increasing role of interlayer vdW interactions, which suppress the inherent in-plane anisotropy by facilitating more isotropic phonon coupling across layers.

3.7. Power-dependent Raman study and calculation of in-plane thermal conductivity

An excitation-power-dependent Raman study was performed on a CVD-grown suspended 2D $ReSe_2$ layer to assess its thermal conductivity. The experiments utilized a 514 nm laser as the excitation source. The suspended configuration was specifically selected to eliminate the heat dissipation that typically occurs in the supported samples, which can compromise the accuracy of in-plane thermal conductivity measurements.[61–63] This configuration ensured that the laser-induced heat was conducted solely through the suspended $ReSe_2$ film, providing a more reliable evaluation of its thermal properties. To evaluate how optical irradiation influences thermal transport in $ReSe_2$, we estimated the change in in-plane thermal conductivity using Raman data. Given that the 1 μm laser spot size is significantly smaller than the hole diameter (~40 μm) of the suspended film holder, heat dissipation can be approximated as radial diffusion from the center of the hole to the edges. For suspended $ReSe_2$, the thermal conductivity (κ) follows Fourier's law: $\kappa = \gamma \cdot \frac{\nabla P}{\nabla T}$, where ∇P is the change in laser power, ∇T is the temperature difference between the excitation spot and the suspended film edge, and γ is a structural factor given by $\gamma = \frac{1}{2\pi t}\ln\left(\frac{R_2}{R_1}\right)$.[66] Here, R_1, R_2, and t represent the laser spot radius, hole diameter, and sample thickness, respectively. Since the Raman peak position of the A_g-like mode shifts linearly with temperature under low laser power, we can rewrite the thermal conductivity expression as:

$$\kappa = \frac{a\alpha}{2\pi t}\ln\left(\frac{R_2}{R_1}\right)\frac{1}{\frac{d\omega}{dP}}$$

where $d\omega/dP$ represents the Raman peak shift per unit laser power, α is the first-order temperature coefficient, and a denotes optical absorption of the sample. The power-dependent Raman spectra for the suspended $ReSe_2$ layer are shown in Fig. 6(c). A systematic redshift in the Raman peak positions with increasing laser power was observed, indicative of localized heating effects. This behavior was analyzed to extract the thermal conductivity of the $ReSe_2$ layer using the established heat diffusion model. This approach underscores the importance of eliminating substrate-induced heat dissipation to obtain accurate measurements of thermal conductivity in 2D materials.[62]

The Raman spectra were fitted using a Lorentzian lineshape to extract the power-dependent frequency shifts accurately. With increasing laser excitation intensity, a systematic redshift in the Raman peak positions was observed, attributed to localized heat generated by the laser. This localized heating enhances phonon–phonon interactions in the system, resulting in both the redshift and a broadening of the Raman linewidth. The broadened linewidth reflects increased vibrational coupling induced by thermal effects. The characteristic shifts of the A_g-like Raman mode at 175 cm^{-1} of 1L-$ReSe_2$ with increasing laser power are shown in Fig. 6(c). The schematics of the power-dependent Raman setup are shown in Fig. S10(a) (SI). The shifts in the out-of-plane mode directly correspond to thermal conduction within the suspended $ReSe_2$ layer, as the heat generated by the laser is entirely conducted through the material without dissipation to a substrate. From the slopes of the plot shown in Fig. 6(d), the frequency shift per unit power ($d\omega/dP$) for 1L-$ReSe_2$ is −0.049 ± 0.0035 cm^{-1} μW^{-1}. Putting the value of $\alpha_\perp$ = −0.0097 ± 0.00030 cm^{-1} K^{-1}, the height of the monolayer is ~0.7 nm, and $a \sim 0.15$[46] in the thermal conductivity formula. Thus, the measured in-plane thermal conductivity for monolayer $ReSe_2$ is 25.2 ± 3.5 Wm^{-1} K^{-1}. Furthermore, for the annealed 1L-A$ReSe_2$, as shown in Fig. S10(b) (SI), the power-dependent Raman spectra depict the introduction of Se vacancies, causing a decrease in the slope ($d\omega/dP$) to −0.0415 ± 0.0012 cm^{-1} μW^{-1}, resulting in a lower in-plane thermal conductivity of 20.7 ± 2.5 Wm^{-1} K^{-1}. For the layer stacking case, 3L-$ReSe_2$, as depicted in Fig. S10(c) (SI), shows a slope of ($d\omega/dP$) −0.0532 ± 0.0092 cm^{-1} μW^{-1} and a value of $a \sim 0.25$,[46] leading to a much lower in-plane thermal conductivity of 10.3 ± 1.8 Wm^{-1} K^{-1}. These values place $ReSe_2$ among the lowest in-plane thermal conductivity materials in the TMD family, as shown in Table 2, underscoring its strong potential for thermoelectric applications and fitting well in the trend of previously reported values.[67] Note that the model used for the in-plane thermal conductivity calculation assumes an isotropic homogeneous medium, while $ReSe_2$ is anisotropic even in the basal plane. In anisotropic 2D materials, such as $PdSe_2$ and $ReSe_2$, the in-plane thermal con-

Table 2 Comparison of the thermal conductivity of CVD-grown isotropic and anisotropic 2D materials using micro-Raman analysis

Material	Thermal conductivity (Wm^{-1} K^{-1})	Ref.
Monolayer graphene	~3600	69
Nine-layer BN	~280	70
Bilayer MoS_2	~15.6	71
Multi-layer MoS_2	~43.4	
Monolayer WS_2	~32	72
Bilayer WS_2	~53	
Monolayer WSe_2	~246	73
Multilayer $MoSe_2$	~28.48	74
Bilayer $PdSe_2$	~36.8	62
Five-layer $PdSe_2$	~10.1	
Monolayer $ReSe_2$	~25.2	This work
Se-vacancy-rich monolayer $ReSe_2$	~20.7	
Trilayer $ReSe_2$	~10.3	

ductivity is usually lower than that of isotropic 2D materials because of the significant difference in bonding strength between the in-plane (strongly bonded) and out-of-plane (weakly bonded) directions, leading to increased phonon scattering when heat tries to transfer through the weaker, out-of-plane direction, effectively hindering heat flow and resulting in a lower overall thermal conductivity. This is a kind of "boundary scattering" due to the limitations imposed by the material layered structure. With the introduction of Se vacancies, these values fall even further. When phonons attempt to travel from one layer to another, they experience frequent scattering at the interface due to the large difference in atomic arrangement, reducing their mean free path and lowering thermal conductivity. It may be noted that the contribution of heat loss to surrounding air molecules during the Raman measurement is not considered here. As a result, the obtained thermal conductivity value may have been overestimated here,[68] in particular for monolayer $ReSe_2$. Nevertheless, these results are crucial for advancing our understanding of temperature-dependent phonon modes in $ReSe_2$, offering valuable insights into phonon–phonon and electron–phonon interactions in this 2D material. It is also important to point that we have used an simplified expression for the calculation of thermal conductivity where we neglected the effect of heat lost to the air, which will further reduce the calculated value.

For our results, it is evident that the in-plane thermal conductivity (κ) of $ReSe_2$ is strongly dependent on both layer thickness and selenium vacancies. We found that, unlike many isotropic 2D materials,[62,75] where κ increases with the number of layers, $ReSe_2$ exhibits an inverse trend, with its in-plane thermal conductivity decreasing from the monolayer to the trilayer. This behavior is attributed to enhanced interlayer interactions, which suppress out-of-plane phonon transport and increase overall phonon scattering in the anisotropic lattice. The introduction of selenium vacancies further reduces κ, as these point defects act as additional scattering centres that impede phonon propagation. These results provide valuable insights into modulating heat transport in anisotropic 2D materials through both structural stacking and defect engineering, reinforcing the potential of $ReSe_2$ for applications in thermal management and nanoscale optoelectronic devices.

3.7. First-principles investigation of lattice dynamics and thermal transport properties using DFT

The optimized lattice constants obtained from our DFT calculations are in excellent agreement with experimental values, confirming the accuracy of our calculation. The obtained lattice parameters for $ReSe_2$ ($a \approx 6.78$ Å, $b \approx 6.66$ Å, and $\gamma \approx 118.86°$) closely match the experimental values ($a \approx 6.76$ Å, $b \approx 6.66$ Å, and $\gamma \approx 118.6°$). This agreement assures that the theoretical framework can reliably predict phonon and lattice thermal conductivity (κ_l).

Fig. 7(a) shows the phonon dispersion of monolayer $ReSe_2$ along with the Brillouin zone and the corresponding high-symmetry paths. The absence of any imaginary frequencies indicates that the structure is dynamically stable. Monolayer $ReSe_2$ possesses 12 atoms in its unit cell (due to its distorted crystal structure), yielding 36 phonon branches in total ($3N$, where $N = 12$). Among these, the three low-lying branches are the acoustic modes: one out-of-plane flexural mode (ZA) and two in-plane modes, transverse acoustic (TA) and longitudinal acoustic (LA). The remaining 33 branches are higher-energy optical phonon modes. As expected for two-dimensional materials, the flexural ZA mode exhibits a quadratic dispersion near the

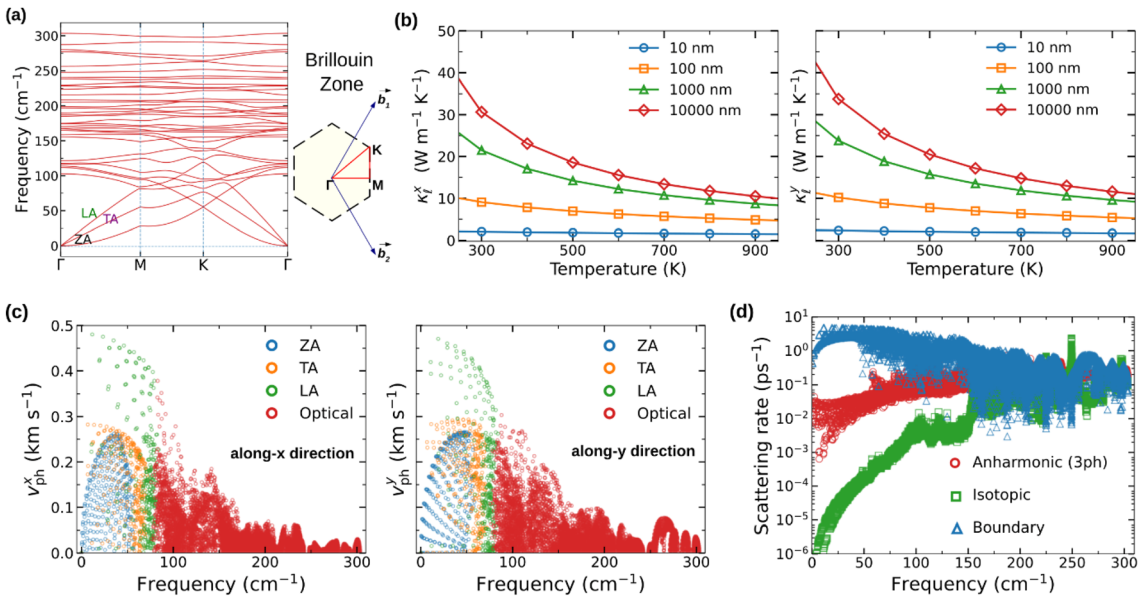

Fig. 7 (a) Phonon dispersion of the $ReSe_2$ monolayer along with the Brillouin zone, highlighting the high symmetry path and reciprocal basis vectors. (b) The lattice thermal conductivity κ_l along the x-direction (κ_l^x) and the y-direction (κ_l^y) as a function of temperature for different sample sizes L. (c) Phonon group velocity along the x-direction and the y-direction. (d) Scattering rates at $T = 300$ K for $L = 1000$ nm.

Brillouin zone center (Γ), whereas the in-plane TA and LA modes show linear dispersion near Γ. This behavior is a well-known characteristic of 2D monolayers.

Importantly, the acoustic phonon branches of $ReSe_2$ are highly anisotropic. In particular, the ZA and TA branches possess a softening feature (lower in frequency) along the Γ–M direction (*x*-direction) compared to the Γ–K direction (*y*-direction). This anisotropic dispersion implies that phonon group velocities will differ between the two in-plane directions, suggesting anisotropic thermal transport. Thus, phonons along the *x*-direction may have lower velocities than those along the *y*-direction, as corroborated below.

Fig. 7(b) displays the lattice thermal conductivity κ_l of monolayer $ReSe_2$ as a function of temperature for various sample sizes *L*. We have calculated the κ_l values for several representative sample sizes (from L = 10 nm up to L = 10 000 nm) to account for boundary scattering effects and to mimic experimental conditions. In typical thermal conductivity measurements on 2D materials using indirect methods such as Raman analysis, the laser spot size or thermal transport distance is on the order of microns, typically ∼1.2 μm (for a 514 nm laser with a 100× short working distance objective), so considering finite sample sizes is important. The κ_l value decreases with increasing temperature for all sample sizes, indicating Umklapp-type phonon scattering. We also observe that the κ_l value increases with increasing sample length *L*: for example, a 1000 nm sample shows a higher thermal conductivity than a 10 nm sample at the same temperature. This trend occurs because small samples experience significant boundary scattering, which limits the phonon mean free path and thus reduces thermal conductivity. As the sample size increases (approaching the quasi-infinite or bulk limit), boundary scattering becomes less significant and the κ_l value increases accordingly.

Quantitatively, our calculations yield room-temperature (300 K) thermal conductivities that agree very well with our experimental observations when the sample size is taken to be in the micron range. For a sample length of L = 1000 nm, we obtain $\kappa_l^x \approx 21.5$ Wm^{-1} K^{-1} along the *x*-direction and $\kappa_l^y \approx 23.8$ Wm^{-1} K^{-1} along the *y*-direction. These values increase to about 30.6 and 33.8 Wm^{-1} K^{-1}, respectively, for a larger sample of L = 10 000 nm. The experimental in-plane thermal conductivity of $ReSe_2$ at 300 K (for a sample with the lateral size on the order of a few microns) is around 25.2 Wm^{-1} K^{-1}. This falls right between our theoretical predictions for L = 1000 nm and L = 10 000 nm, indicating excellent consistency. The agreement suggests that our first-principles approach, combined with the phonon Boltzmann transport equation, successfully captures the key phonon scattering processes and size effects relevant to the experimental setup.

Another noteworthy result is the difference between κ_l along the two principal in-plane directions of monolayer $ReSe_2$. It is lower along the *x*-direction than along the *y*-direction, reflecting the anisotropic phonon dispersion. As shown in Fig. 7(c), the phonon group velocity v_{ph} of the acoustic modes is smaller along the *x*-direction than along the *y*-direction. Since $\kappa_l \propto C$ v_{ph} τ, a lower v_{ph} value along the *x*-direction yields a lower κ_l value. High-frequency optical phonons, having a very small group velocity and short mean free paths, contribute negligibly, so in-plane heat transport is dominated by acoustic phonons and a few low-lying optical modes whose anisotropic dispersion gives rise to anisotropic κ_l. Finally, it is important to note that our first-principles BTE calculations of thermal conductivity include only intrinsic three-phonon scattering and boundary scattering in determining phonon lifetimes. Extrinsic mechanisms—such as isotopic disorder, point defects, vacancies, impurities, and interface-induced scattering—are not included here. Therefore, these reported κ_l values represent an upper bound within the current theoretical framework.

Fig. 7(d) shows the phonon scattering rates as a function of phonon frequency for a 1000 nm sample at 300 K. At low frequencies (below ∼50 cm^{-1}), boundary scattering predominantly limits the phonon lifetime, as long-wavelength acoustic phonons can readily reach the sample boundaries and be scattered. In the intermediate frequency range, intrinsic three-phonon processes become increasingly significant. At high frequencies (optical phonon range), boundary scattering, three-phonon scattering, and isotopic scattering contribute nearly equally to limiting phonon lifetimes.

To reduce the computational cost, we have limited our calculations to a monolayer only. However, based on our analysis of phonon scattering, we can anticipate changes in thermal transport when moving from a monolayer to thicker samples (*e.g.*, bilayer or trilayer $ReSe_2$). In few-layer samples, additional phonon scattering channels arise from interlayer interactions. The presence of multiple layers introduces more interfaces (*e.g.*, layer–layer boundaries) and additional vibrational modes, such as layer shear and layer breathing modes, which enhance phonon scattering. Consequently, both boundary-like scattering (at external surfaces and interfaces) and intrinsic three-phonon scattering are expected to increase in multilayer $ReSe_2$. This would further reduce κ_l in thicker samples, consistent with the trends observed in other two-dimensional materials.[76,77] Apart from layer-dependent effects, point defects such as Se vacancies can further lower κ_l by enhancing phonon scattering. Similar to S vacancies in MoS2,[78] the removal of a chalcogen atom perturbs the local mass distribution and interatomic force constants through variation in bond lengths and strength, thereby increasing the lattice anharmonicity and scattering rates of heat-carrying phonons. These theoretical expectations qualitatively support experimental observations that multilayer Se-vacancy-containing $ReSe_2$ samples exhibit lower thermal conductivity than the monolayer, as increased scattering diminishes the phonon heat-carrying efficiency.

Our first-principles calculations offer a comprehensive understanding of lattice dynamics and thermal transport in $ReSe_2$ monolayers, validating and complementing experimental findings. The results provide theoretical support for the measurements and offer deeper insights into how phonon dispersion and scattering mechanisms govern the material's anisotropic thermal conductivity.

4. Conclusion

In essence, we conducted an in-depth analysis of CVD-grown $ReSe_2$, a highly anisotropic 2D material, to evaluate its structural, thermal, and vibrational properties using low-temperature Raman spectroscopy. Our findings reveal two distinct pathways for modulating the thermal properties of 2D $ReSe_2$, *i.e.*, *via* defect creation and layer stacking. For the annealed monolayer $ReSe_2$, the introduction of selenium vacancies resulted in a redshift of the Raman peaks. This redshift is indicative of an n-type doping effect caused by the Se vacancies. Crucially, the temperature coefficients for both modes in the annealed sample decreased compared to the pristine monolayer, which reflects a reduction in phonon–phonon interactions due to the enhanced phonon scattering from the newly introduced defect sites. The Raman spectrum of trilayer $ReSe_2$ exhibited a redshift of characteristic peaks compared to monolayer $ReSe_2$, which we attribute to weak interlayer vdW interactions. Furthermore, the first-order temperature coefficients (α) showed contrasting trends with increasing layer number, reinforcing the material's anisotropy. Specifically, the coefficient for the in-plane E_g-like mode slightly increased, while the coefficient for the out-of-plane A_g-like mode decreased. This behavior is a direct consequence of enhanced interlayer coupling, which restricts out-of-plane vibrations and alters phonon–phonon interactions. Using power-dependent Raman measurement, we determined the thermal conductivity (κ) of ~25.2 Wm^{-1} K^{-1} for the monolayer and ~10.3 Wm^{-1} K^{-1} for the trilayer, confirming a decreasing trend with increasing layer thickness. Furthermore, the anisotropic ratio, a direct measure of in-plane anisotropy, was found to be a giant 6.23 for the monolayer and it decreased to 3.82 for the trilayer. Critically, we demonstrated that the introduction of selenium vacancies further modulates these properties, reducing the thermal conductivity to ~20.7 Wm^{-1} K^{-1} and the anisotropic ratio to ~4.42. These findings are also in excellent agreement with our first-principles calculations using DFT and the phonon Boltzmann transport formalism. Our calculations provide an in-depth understanding of the phonon scattering process and the anisotropic thermal transport behaviour in pristine monolayer $ReSe_2$ and have also enabled us to understand the thermal transport behaviour in multilayer and defect-rich $ReSe_2$ systems. These findings provide crucial insights into phonon–phonon interactions and thermal transport in $ReSe_2$, reinforcing its potential for applications in optoelectronics, thermal management, and sensing. The precise methodologies employed here establish a strong foundation for future investigations into the tunable properties of anisotropic 2D materials.

Author contributions

S. A. designed the experiments, performed conceptualization, visualization, CVD growth, Raman measurements, including power-, polarization-, and temperature-dependent analyses, data curation, formal analysis, and interpretation of results, and wrote the first draft. S. G. helped in experiments, data curation, formal analysis, review, and editing. H. M. performed DFT simulations, formal analysis, review, and editing. R. C. helped in experiments, data curation, formal analysis, review, and editing. R. K. B. helped in data curation, formal analysis, review, and editing. V. V. performed the HADAF-STEM characterization, formal analysis, review, and editing. L. V. performed the Auger spectroscopy measurements, formal analysis, review, and editing. S. G. contributed to writing – review & editing, validation, and investigation. P. K. G. supervised the project, performed data analysis, and interpretation of the results, funding acquisition, investigation, review, and editing.

Conflicts of interest

The authors declare that they have no known competing financial interests or personal relationships that could have appeared to influence the work reported in this paper.

Data availability

The data supporting this article have been included as part of the supplementary information (SI). Supplementary information: supplementary figures including schematic representations, optical images, spectroscopic analyses, and microscopic characterization studies that support the main findings of the study. The schematics illustrate the temperature profile for $ReSe_2$ synthesis and the transfer process onto a TEM grid. The optical images reveal the morphology variations of CVD-grown $ReSe_2$ at different growth temperatures, while the Raman spectra confirm the presence of all 18 Raman-active modes in the 1L-$ReSe_2$, 1L-A$ReSe_2$, and 3L-$ReSe_2$ samples, accompanied by tables detailing various Raman modes and their corresponding positions. Additionally, XPS survey spectra of the as-grown CVD $ReSe_2$ and high-resolution binding energy spectra of C 1s. Comparative table for the FWHM of 1L-$ReSe_2$ and core Re and Se XPS spectra of 1L-A$ReSe_2$. STEM-ADF imaging and line profile analysis further verify vacancy and atomic arrangements in $ReSe_2$ along with EDS and SAED analyses of the freestanding $ReSe_2$ monolayer. Comparison table of the thermal expansion coefficient of $ReSe_2$ with other 2D materials. Schematic representation of E_g-like and A_g-like mode vibrations. Polarization-dependent Raman spectra of 1L-$ReSe_2$, 1L-A$ReSe_2$ and 3L-$ReSe_2$. Power-dependent Raman measurement setup. Raman shifts with varying laser powers for 1L-A$ReSe_2$ and 3L-$ReSe_2$. See DOI: https://doi.org/10.1039/d5nr03668b.

Acknowledgements

The author(s) acknowledge financial support from MEITY (Grant No. 5(1)/2022-NANO). The central instrumental facility at IIT Guwahati is acknowledged for providing AFM, Raman,

and XPS characterization support. Additionally, the National Scholarship Programme (NSP) of the Slovak Republic is acknowledged for supporting the research stay at the Centre for Nanodiagnostics, MTF, STU, Slovakia. The authors gratefully acknowledge the Department of Science and Technology, India, for the computational facilities under Grant No. SR/FST/P-II/020/2009 and IIT Guwahati for the PARAM supercomputing facility.

References

1 J. An, X. Zhao, Y. Zhang, M. Liu, J. Yuan, X. Sun, Z. Zhang, B. Wang, S. Li and D. Li, *Adv. Funct. Mater.*, 2022, **32**, 2110119.
2 T. G. Novak, K. Kim and S. Jeon, *Nanoscale*, 2019, **11**, 19684–19699.
3 M. V. Sulleiro, A. Dominguez-Alfaro, N. Alegret, A. Silvestri and I. J. Gómez, *Sens. Bio-Sens. Res.*, 2022, **38**, 100540.
4 J. Zeb Hassan, A. Raza, Z. U. D. Babar, U. Qumar, N. Tolbert Kaner and A. Cassinese, *J. Mater. Chem. A*, 2023, **11**, 6016–6063.
5 H. Tao, Q. Fan, T. Ma, S. Liu, H. Gysling, J. Texter, F. Guo and Z. Sun, *Prog. Mater. Sci.*, 2020, **111**, 100637.
6 M. Sang, J. Shin, K. Kim and K. J. Yu, *Nanomaterials*, 2019, **9**, 374.
7 M. H. Kalantari and X. Zhang, *Nanomaterials*, 2023, **13**, 117.
8 Q. Ma, G. Ren, K. Xu and J. Z. Ou, *Adv. Opt. Mater.*, 2021, **9**, 2001313.
9 A. N. Rudenko and M. I. Katsnelson, *2D Mater.*, 2024, **11**, 042002.
10 S. Jiang, M. Hong, W. Wei, L. Zhao, N. Zhang, Z. Zhang, P. Yang, N. Gao, X. Zhou, C. Xie, J. Shi, Y. Huan, L. Tong, J. Zhao, Q. Zhang, Q. Fu and Y. Zhang, *Commun. Chem.*, 2018, **1**, 1–8.
11 S. Song, G. Zhang, J. Qiao, B. Chen, M. Shen, X. Yuan, M. G. Somekh and F. Feng, *Phys. B*, 2023, **663**, 415000.
12 K. Li, C. Du, H. Gao, T. Yin, L. Zheng, J. Leng and W. Wang, *ACS Appl. Mater. Interfaces*, 2022, **14**, 33589–33597.
13 X. Tian and Y. Liu, *J. Semicond.*, 2021, **42**, 032001.
14 N. Wang, B. Lu, X. Qi, Y. Jiao, Z. Wen, H. Chen and J. Bai, *Opt. Laser Technol.*, 2019, **116**, 300–304.
15 Y. Pan, T. Zheng, F. Gao, L. Qi, W. Gao, J. Zhang, L. Li, K. An, H. Gu and H. Chen, *Small*, 2024, **20**, 2311606.
16 A. Mikhin, A. Shubnic, T. Ivanova, I. Shelykh, A. K. Samusev and I. Iorsh, *ACS Photonics*, 2023, **10**, 1769–1774.
17 L. Du, G. Jiang, L. Miao, B. Huang, J. Yi, C. Zhao and S. Wen, *Opt. Mater. Express*, 2018, **8**, 926–935.
18 N. R. Pradhan, C. Garcia, B. Isenberg, D. Rhodes, S. Feng, S. Memaran, Y. Xin, A. McCreary, A. R. H. Walker, A. Raeliarijaona, H. Terrones, M. Terrones, S. McGill and L. Balicas, *Sci. Rep.*, 2018, **8**, 12745.
19 V. Adepu, M. Tathacharya, C. S. Raghuram and P. Sahatiya, *J. Micromech. Microeng.*, 2023, **33**, 115007.
20 B. Kang, Y. Kim, J. H. Cho and C. Lee, *2D Mater.*, 2017, **4**, 025014.
21 E. Zhang, P. Wang, Z. Li, H. Wang, C. Song, C. Huang, Z.-G. Chen, L. Yang, K. Zhang, S. Lu, W. Wang, S. Liu, H. Fang, X. Zhou, H. Yan, J. Zou, X. Wan, P. Zhou, W. Hu and F. Xiu, *ACS Nano*, 2016, **10**, 8067–8077.
22 H. Wang, E. Liu, Y. Wang, B. Wan, C.-H. Ho, F. Miao and X. G. Wan, *Phys. Rev. B*, 2017, **96**, 165418.
23 L. Deng, X. Zhang, J. Liu, A. Wei, Y. D. He, Z. Liu and N. Luo, *Phys. Chem. Chem. Phys.*, 2022, **24**, 14479–14487.
24 A. Pandey, R. Verma and A. Srivastava, *New J. Chem.*, 2023, **47**, 12983–12991.
25 J. Ran, L. Chen, D. Wang, A. Talebian-Kiakalaieh, Y. Jiao, M. A. Hamza, Y. Qu, L. Jing, K. Davey and S.-Z. Qiao, *Adv. Mater.*, 2023, **35**, 2210164.
26 M. Zhuang, G.-L. Xu, L.-Y. Gan, Y. Dou, C.-J. Sun, X. Ou, Y. Xie, Z. Liu, Y. Cai and Y. Ding, *Nano Energy*, 2019, **58**, 660–668.
27 Y. Li, Z. Luo, Y. Song, X. Weng, Y. Wang, L. Liu, J. Song, J. Qu, X. Peng and Y. Yuan, *Opt. Lasers Eng.*, 2023, **171**, 107817.
28 Y. Li, Z. Luo, Y. Song, Y. Yuan, X. Peng, J. Song and J. Qu, *Sens. Actuators, B*, 2022, **362**, 131781.
29 Z. Xia, X. Chen, H. Ci, Z. Fan, Y. Yi, W. Yin, N. Wei, J. Cai, Y. Zhang and J. Sun, *J. Energy Chem.*, 2021, **53**, 155–162.
30 M. F. Khan, S. Rehman, I. Akhtar, S. Aftab, H. M. S. Ajmal, W. Khan, D. Kim and J. Eom, *2D Mater.*, 2019, **7**, 015010.
31 E. Faella, K. Intonti, L. Viscardi, F. Giubileo, A. Kumar, H. T. Lam, K. Anastasiou, M. F. Craciun, S. Russo and A. Di Bartolomeo, *Nanomaterials*, 2022, **12**, 1886.
32 S. Kim, C. Lee, Y. S. Lim and J.-H. Shim, *ACS Omega*, 2021, **6**, 278–283.
33 M.-C. Chang, P.-H. Ho, M.-F. Tseng, F.-Y. Lin, C.-H. Hou, I.-K. Lin, H. Wang, P.-P. Huang, C.-H. Chiang, Y.-C. Yang, I.-T. Wang, H.-Y. Du, C.-Y. Wen, J.-J. Shyue, C.-W. Chen, K.-H. Chen, P.-W. Chiu and L.-C. Chen, *Nat. Commun.*, 2020, **11**, 3682.
34 W. Yang, Y. Mu, X. Chen, N. Jin, J. Song, J. Chen, L. Dong, C. Liu, W. Xuan, C. Zhou, C. Cong, J. Shang, S. He, G. Wang and J. Li, *Discover Nano*, 2023, **18**, 13.
35 Y. Yan, L. Chen, K. Dai, Y. Li, L. Wang, K. Jiang, A. Cui, J. Zhang and Z. Hu, *J. Phys. Chem. Lett.*, 2023, **14**, 7618–7625.
36 P. Hohenberg and W. Kohn, *Phys. Rev.*, 1964, **136**, B864–B871.
37 W. Kohn and L. J. Sham, *Phys. Rev.*, 1965, **140**, A1133–A1138.
38 G. Kresse and J. Furthmüller, *Phys. Rev. B: Condens. Matter Mater. Phys.*, 1996, **54**, 11169–11186.
39 P. E. Blöchl, *Phys. Rev. B: Condens. Matter Mater. Phys.*, 1994, **50**, 17953–17979.
40 J. P. Perdew, K. Burke and M. Ernzerhof, *Phys. Rev. Lett.*, 1996, **77**, 3865–3868.
41 H. J. Monkhorst and J. D. Pack, *Phys. Rev. B*, 1976, **13**, 5188–5192.
42 A. Togo and I. Tanaka, *Scr. Mater.*, 2015, **108**, 1–5.
43 W. Li, J. Carrete, N. A. Katcho and N. Mingo, *Comput. Phys. Commun.*, 2014, **185**, 1747–1758.

44 J. Zhang, Z. Zhao, M. Jiang, Y. Cheng and G. Zhang, *Phys. Rev. Mater.*, 2025, **9**, 094603.
45 G. Nam, S. Park, K. Heo, J. Bong, D. Lee, H. Kim, K. M. Ponnusamy, H. Bae, H. G. Park, J.-H. Lee and H.-S. Jang, *JPhys Mater.*, 2024, **7**, 045005.
46 Y. Ge, C. Lu, Q. Zhao, M. Luo, Y. Liu, T. Han, Y. Zhou and X. Xu, *Phys. Rev. Appl.*, 2022, **18**, 034050.
47 G. C. Resende, G. A. S. Ribeiro, O. J. Silveira, J. S. Lemos, J. C. Brant, D. Rhodes, L. Balicas, M. Terrones, M. S. C. Mazzoni, C. Fantini, B. R. Carvalho and M. A. Pimenta, *2D Mater.*, 2020, **8**, 025002.
48 S. Jiang, J. Yang, Y. Shi, J. Zhao, C. Xie, L. Zhao, J. Fu, P. Yang, Y. Huan, Q. Xie, H. Jiang, Q. Zhang, X. Wang, F. Su and Y. Zhang, *Nano Res.*, 2020, **13**, 667–675.
49 Ł. Kipczak, M. Grzeszczyk, K. Olkowska-Pucko, A. Babiński and M. R. Molas, *J. Appl. Phys.*, 2020, **128**, 044302.
50 D. A. Chenet, B. Aslan, P. Y. Huang, C. Fan, A. M. van der Zande, T. F. Heinz and J. C. Hone, *Nano Lett.*, 2015, **15**, 5667–5672.
51 H. Zhao, J. Wu, H. Zhong, Q. Guo, X. Wang, F. Xia, L. Yang, P. Tan and H. Wang, *Nano Res.*, 2015, **8**, 3651–3661.
52 Q. Shi, E. Shih, D. Rhodes, B. Kim, K. Barmak, K. Watanabe, T. Taniguchi, Z. Papic, D. Abanin, J. Hone and C. Dean, *Nat. Nanotechnol.*, 2022, **17**, 577–582.
53 S.-H. Jo, H.-Y. Park, D.-H. Kang, J. Shim, J. Jeon, S. Choi, M. Kim, Y. Park, J. Lee, Y. J. Song, S. Lee and J.-H. Park, *Adv. Mater.*, 2016, **28**, 6711–6718.
54 M. H. Ali, D.-H. Kang and J.-H. Park, *Org. Electron.*, 2018, **53**, 14–19.
55 F. Cui, X. Li, Q. Feng, J. Yin, L. Zhou, D. Liu, K. Liu, X. He, X. Liang, S. Liu, Z. Lei, Z. Liu, H. Peng, J. Zhang, J. Kong and H. Xu, *Nano Res.*, 2017, **10**, 2732–2742.
56 F. Cui, X. Li, Q. Feng, J. Yin, L. Zhou, D. Liu, K. Liu, X. He, X. Liang, S. Liu, Z. Lei, Z. Liu, H. Peng, J. Zhang, J. Kong and H. Xu, *Nano Res.*, 2017, **10**, 2732–2742.
57 L. Xing, X. Yan, J. Zheng, G. Xu, Z. Lu, L. Liu, J. Wang, P. Wang, X. Pan and L. Jiao, *InfoMat*, 2019, **1**, 552–558.
58 R. Kosiba, J. Liday, G. Ecke, O. Ambacher, J. Breza and P. Vogrinčič, *Vacuum*, 2006, **80**, 990–995.
59 Y. Zhu, L. Tao, X. Chen, Y. Ma, S. Ning, J. Zhou, X. Zhao, M. Bosman, Z. Liu, S. Du, S. T. Pantelides and W. Zhou, *iScience*, 2021, **24**(12), 103456.
60 X. Chen, B. Lei, Y. Zhu, J. Zhou, M. Gao, Z. Liu, W. Ji and W. Zhou, *ACS Mater. Lett.*, 2021, **3**, 1513–1520.
61 M. T. Hossain and P. K. Giri, *J. Appl. Phys.*, 2021, **129**, 175102.
62 T. Jena, M. T. Hossain and P. K. Giri, *J. Mater. Chem. C*, 2021, **9**, 16693–16708.
63 R. Chahal, A. Bora and P. K. Giri, *ACS Appl. Energy Mater.*, 2023, **6**(17), 8794–8807.
64 Z. Lin, W. Liu, S. Tian, K. Zhu, Y. Huang and Y. Yang, *Sci. Rep.*, 2021, **11**, 7037.
65 S. Song, G. Zhang, J. Qiao, B. Chen, M. Shen, X. Yuan, M. G. Somekh and F. Feng, *Phys. B*, 2023, **663**, 415000.
66 C. Shen, W. Du, Z. Wu, J. Xing, S. T. Ha, Q. Shang, W. Xu, Q. Xiong, X. Liu and Q. Zhang, *Nanoscale*, 2017, **9**, 8281–8287.
67 S. Tahbaz and A. Pisana, *JPhys Mater.*, 2024, **7**, 015014.
68 D. S. Reig, S. Varghese, R. Farris, A. Block, J. D. Mehew, O. Hellman, P. Woźniak, M. Sledzinska, A. E. Sachat, E. Chávez-Ángel, S. O. Valenzuela, N. F. van Hulst, P. Ordejón, Z. Zanolli, C. M. S. Torres, M. J. Verstraete and K.-J. Tielrooij, *Adv. Mater.*, 2022, **34**, 2108352.
69 W. Cai, A. L. Moore, Y. Zhu, X. Li, S. Chen, L. Shi and R. S. Ruoff, *Nano Lett.*, 2010, **10**, 1645–1651.
70 H. Zhou, J. Zhu, Z. Liu, Z. Yan, X. Fan, J. Lin, G. Wang, Q. Yan, T. Yu, P. M. Ajayan and J. M. Tour, *Nano Res.*, 2014, **7**, 1232–1240.
71 J. J. Bae, H. Y. Jeong, G. H. Han, J. Kim, H. Kim, M. S. Kim, B. H. Moon, S. C. Lim and Y. H. Lee, *Nanoscale*, 2017, **9**, 2541–2547.
72 N. Peimyoo, J. Shang, W. Yang, Y. Wang, C. Cong and T. Yu, *Nano Res.*, 2015, **8**, 1210–1221.
73 S. Rai and A. Srivastava, *J. Appl. Phys.*, 2024, **136**, 154301.
74 J. Sun, K. Dai, W. Xia, J. Chen, K. Jiang, Y. Li, J. Zhang, L. Zhu, L. Shang, Z. Hu and J. Chu, *ACS Omega*, 2021, **6**, 30526–30533.
75 L. Pi, L. Li, X. Hu, S. Zhou, H. Li and T. Zhai, *Nanotechnology*, 2018, **29**, 505709.
76 X. Gu, B. Li and R. Yang, *J. Appl. Phys.*, 2016, **119**, 085106.
77 T. Miao, M. Xiang, D. Chen, M. An and W. Ma, *Int. J. Heat Mass Transfer*, 2022, **183**, 122099.
78 C. A. Polanco, T. Pandey, T. Berlijn and L. Lindsay, *Phys. Rev. Mater.*, 2020, **4**, 014004.